# nature nanotechnology

Article

https://doi.org/10.1038/s41565-023-01542-9

# Reversible optical data storage below the diffraction limit

Received: 31 October 2022

Richard Monge **1**,2,3, Tom Delord **1**,3 & Carlos A. Meriles **1**,2

Accepted: 18 September 2023

Published online: 4 December 2023



Colour centres in wide-bandgap semiconductors feature metastable charge states that can be interconverted with the help of optical excitation at select wavelengths. The distinct fluorescence and spin properties in each of these states have been exploited to show storage of classical information in three dimensions, but the memory capacity of these platforms has been thus far limited by optical diffraction. Here we leverage local heterogeneity in the optical transitions of colour centres in diamond (nitrogen vacancies) to demonstrate selective charge state control of individual point defects sharing the same diffraction-limited volume. Further, we apply this approach to dense colour centre ensembles, and show rewritable, multiplexed data storage with an areal density of 21 Gb inch<sup>-2</sup> at cryogenic temperatures. These results highlight the advantages for developing alternative optical storage device concepts that can lead to increased storage capacity and reduced energy consumption per operation.

Wide-bandgap semiconductors host impurities and other point defects whose absorption at select optical wavelengths is known to confer signature hues on gems. These 'colour centres' can take different charge states, each featuring characteristic optical and spin properties. Relevant examples are the nitrogen-vacancy (NV) and silicon-vacancy (SiV) centres in diamond, or the di-vacancy and SiV centres in silicon carbide, presently attracting interest for applications in quantum information processing and nanoscale sensing<sup>1,2</sup>. Laser illumination at select wavelengths induces ionization and recombination processes that can drive the colour centre into desired states of charge almost deterministically<sup>3</sup>. The injection of carriers produced by light-driven colour centres serves as a tool to probe charge capture down to individual point defects<sup>4</sup>, as a mechanism for the electrical read-out of spin qubits<sup>5</sup> or as route to expose non-fluorescent charge emitters in a solid<sup>6</sup>; spin-to-charge conversion has also emerged as a strategy to enhance spin read-out sensitivity<sup>7-11</sup>. Since the thermal activation of deep donors or acceptors is negligible in insulators, excess trapped charges have long lifetimes, especially at low and moderate concentrations where inter-defect carrier tunnelling is suppressed. Colour centres can therefore be seen as atomic-size optical memories, a notion already exploited to demonstrate reversible, three-dimensional data storage<sup>12-14</sup>.

An important hurdle impacting colour centre charge control is light diffraction, limiting spatial discrimination to hundreds of

nanometres. Colour centre imaging with precision down to a few nanometres can be attained via super-resolution techniques such as stimulated emission depletion<sup>15</sup> (STED) or stochastic optical reconstruction microscopy<sup>16,17</sup> (STORM). Unfortunately, applying these methods to sub-diffraction charge control is impractical, either because the illumination intensity is too weak to induce controllable charge state conversion—as in STORM—or because the finite, diffraction-limited size of the STED beam unavoidably alters the charge state of colour centres proximal to a target<sup>18–20</sup>. Several STED-based approaches to sub-diffraction optical lithography have been demonstrated in the recent past<sup>21–26</sup>, but the photo-chemical reactions this method relies on are non-reversible, require careful beam alignment and are often limited to two dimensions.

Here we implement charge control protocols in NV centres in diamond under cryogenic conditions, where narrow optical transitions reveal the fine structure in the ground and first excited states <sup>27</sup>. We first focus on small sets of colour centres within the same diffraction-limited volume and show charge state preparation of individual NVs using selective, local-field-shifted optical transitions. Switching to denser ensembles where individual control becomes impractical, we nonetheless demonstrate the charge state writing and read-out of frequency-binned NV subsets within the same focal volume, which we then exploit to show multiplexed data storage on the optical plane.

<sup>1</sup>Department of Physics, City College of New York, CUNY, New York, NY, USA. <sup>2</sup>Graduate Center, CUNY, New York, NY, USA. <sup>3</sup>These authors contributed equally: Richard Monge, Tom Delord. —e-mail: cmeriles@ccny.cuny.edu

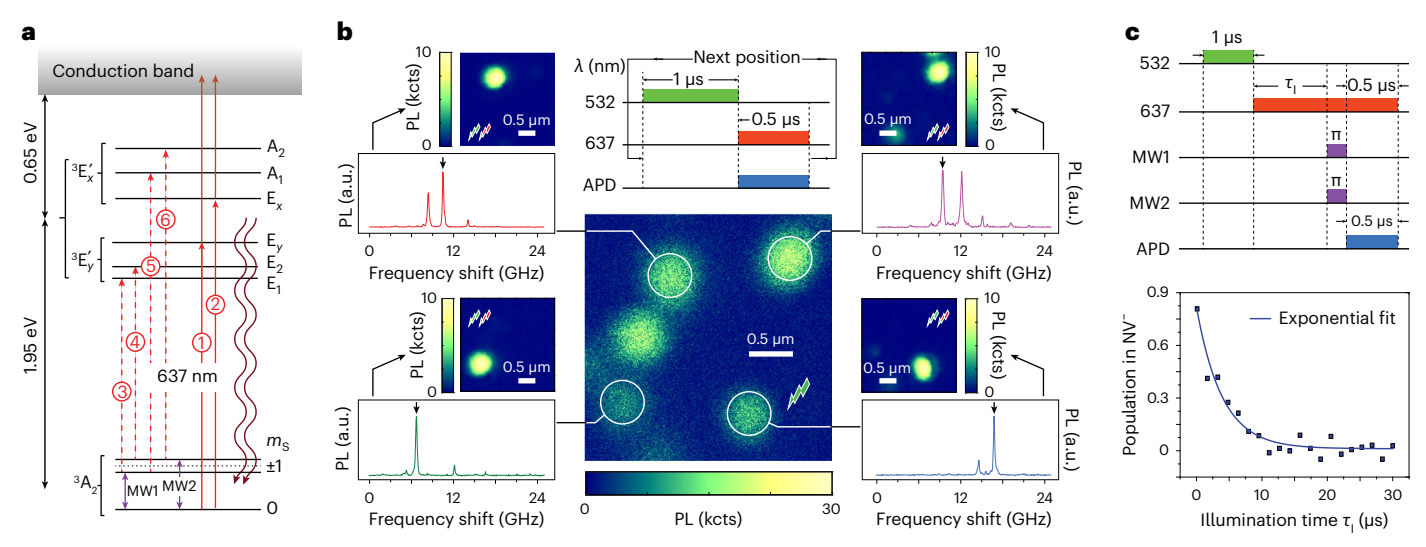


**Fig. 1**| **Optical spectroscopy and charge control of NV**<sup>-</sup> **centres under cryogenic conditions. a**, Energy level diagram of NV<sup>-</sup>. Light red arrows (solid and dashed) indicate optical transitions around 637 nm between levels in the ground and first excited manifolds; dark red arrows indicate ionization photons, and wavy arrows denote emitted photons. b, Scanning confocal image under green excitation of a section of the crystal featuring multiple NVs. The insets at the sides show the optical spectra of the circled NVs in the set upon application of the protocol in the upper diagram using red illumination of variable frequency; here (and everywhere else unless noted), the horizontal axis is a frequency shift relative to 470.470 THz. For each case, we obtain a NV-selective image using

the same protocol but with the 637 nm laser tuned to one of the  $S_z$  transitions (indicated by an arrow in each spectrum); only the resonant NV is visible in the images. The laser powers are 1.6 mW and 2  $\mu$ W at 532 and 637 nm, respectively. **c**, NV ionization protocol under strong optical excitation (210  $\mu$ W) at 637 nm (top). MW1 (MW2) denotes MW excitation resonant with the  $m_s=0 \leftrightarrow m_s=-1$  ( $m_s=0 \leftrightarrow m_s=+1$ ) transition in the ground state triplet; the duration of the  $\pi$ -pulses is 100 ns. Relative NV charge state population as a function of the ionization interval  $\tau_1$  for a representative NV in the set (bottom). All experiments are carried out at 7 K. PL, photoluminescence; a.u., arbitrary units;  $\lambda$ , wavelength; APD, avalanche photo-detector; kcts, kilo-counts.

# **NV-selective imaging**

Figure 1a shows the energy level structure of the negatively charged NV (NV<sup>-</sup>), featuring a triplet  $A_2$  ground state with spin sublevels  $m_s = 0, \pm 1$ , and an excited state manifold combining a spin triplet and an orbital doublet  $E_{x,y}$  (refs. 27,28). We obtain excitation spectra by recording the Stokes-shifted NV<sup>-</sup> emission as we sweep the frequency of a 637 nm, narrow-band laser. Six optical resonances connect the ground and excited state levels with the same spin projection; state hybridization in the excited manifold, however, leads to spin flips that quickly render the NV non-resonant, hence preventing the observation of most transitions in single-wavelength excitation experiments<sup>27</sup>.

One route to circumvent this problem is to accompany laser illumination with microwave (MW) excitation resonant with the two NV spin transitions of the ground state triplet 11,27. Here we follow a different route where pulses of resonant optical excitation near 637 nm alternate with intervals of 532 nm laser light to periodically repump  $NV^-$  into  $m_s = 0$  and recharge  $NV^0$  into  $NV^-$  in the event of ionization. We demonstrate this strategy in Fig. 1b for a set of NVs in a type 2a [100] diamond (crystal A). Confocal microscopy under green illumination (central image) reveals a discrete collection of NVs whose optical spectra we record using the protocol in the upper diagram. Importantly, all NVs exhibit strain- or electric-field-shifted optical resonances<sup>29,30</sup> that we address individually to reconstruct NV-selective images. We illustrate the idea for four emitters in the set, in each case configuring the detection protocol so that the 637 nm laser is resonant with an individual  $S_z(m_s = 0)$  transition. Similar to experiments with SiV centres<sup>31</sup>, the images we obtain highlight almost exclusively the chosen NV, a combined consequence of the laser selectivity and spectral heterogeneity produced by local electric and strain fields (Supplementary Section 1). Remarkably, resonant optical excitation occasionally reveals NVs not observable via green illumination (for example, upper right inset in Fig. 1b), partially a consequence of the NV fluorescence sensitivity to the incoming beam polarization (Supplementary Section 2).

To gain single NV charge state control, we bring the laser frequency on-resonance with one of the cycling transitions ( $m_{\rm s}=0$ ) and increase the power to induce NV $^-$  ionization on a timescale faster than the inverse spin flipping rate (upper schematic in Fig. 1c). We confirm this condition through the application of inversion MW pulses resonant with each of the two NV $^-$  spin transitions at the applied magnetic field ( $B=4.51\pm0.05~\rm mT$ ; Methods); negligible fluorescence upon spin inversion signals NV $^-$ ionization.

#### **Sub-diffraction ionization of individual NVs**

Figure 2a highlights a diffraction-limited site in the crystal hosting a pair of NVs, a composition we infer from the multipeaked structure of the optically detected magnetic resonance (ODMR) spectrum (upper right inset). We separately visualize each NV in the pair by repeatedly imaging the fluorescence pattern from either emitter under selective excitation and subsequently fitting the result with a Gaussian point spread function  $^{32}$ . When combined, the dataset reveals two NVs—referred to as NV<sub>A</sub> and NV<sub>B</sub>—oriented along non-equivalent crystalline axes and separated by an in-plane distance of 90 nm, below optical resolution (-300 nm).

Optical spectroscopy of the same crystal site shows a collection of resonances, each associated with one emitter in the pair or the other. To separate these resonances, we follow the protocol in Fig. 1b, except that we intercalate MW spin inversion pulses between the green and red laser excitation intervals, selectively acting only on one of the two emitters (upper two traces in the optical spectra of Fig. 2a). Comparing the system response in the absence of MW excitation (lower trace) allows us to assign all optical resonances in the pair.

To demonstrate sub-diffraction NV $^-$  charge control, we make the red laser frequency resonant with one of the  $m_s = 0$  transitions in either NV and adjust the illumination intensity and duration to quickly produce ionization. We probe the ensuing charge state of the pair via an ODMR protocol and obtain spectra where the observable dip is contingent on the chosen excitation frequency of the 637 nm laser (middle and lower traces in the plot of Fig. 2b); comparison with the

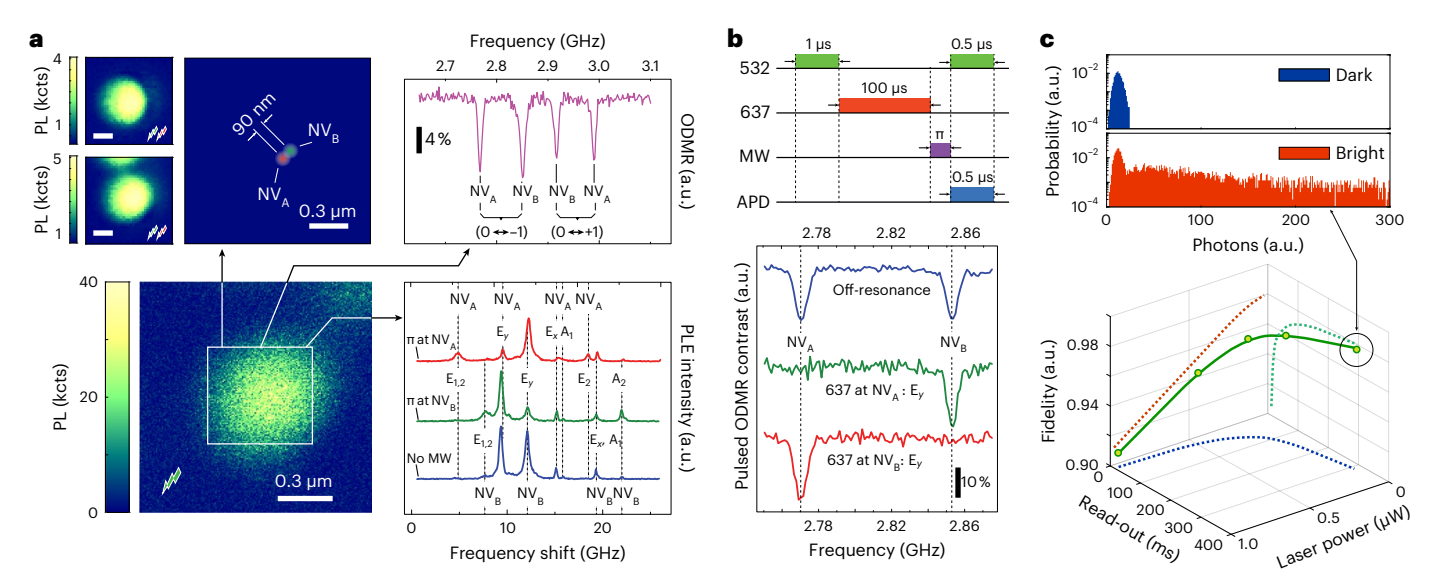


**Fig. 2** | **Sub-diffraction NV**<sup>-</sup> **ionization and read-out. a**, Confocal microscopy under 532 nm illumination of a diamond site containing two NVs (bottom left). The top left insets show NV-selective imaging using the protocol in Fig. 1b and the reconstructed sub-diffraction map as derived from Gaussian point-spreadfunction fits; the red and green coloured circles indicate the mean positions and standard deviations obtained from comparing multiple images over time. The top right inset shows the ODMR spectrum under 532 nm excitation; the four resonances we observe confirm the presence of two differently oriented NVs. The bottom right inset shows NV<sup>-</sup> optical spectroscopy in the absence of MW (blue trace) or upon intercalating a MW π-pulse between the laser pulses in the protocol of Fig. 1b; the MW frequency is chosen resonant with the spin transitions of NV<sub>A</sub> or NV<sub>B</sub> (green and red traces, respectively). **b**, NV-selective ionization protocol (top); for inspection, we reconstruct an ODMR spectrum

(bottom) by varying the MW frequency of the  $\pi$ -pulse (set to probe a band around the  $|0\rangle\leftrightarrow|-1\rangle$  transition). We ionize NV<sub>A</sub> or NV<sub>B</sub> by bringing the 210  $\mu$ W red laser on-resonance with the E<sub>y</sub> transition of either colour centre (green and red traces, respectively); we recover the full ODMR spectrum when the 637 nm laser is tuned away from all transition frequencies. In **a** and **b**, spectra have been displaced vertically for clarity. **c**, Measured charge state read-out fidelity for NV<sub>A</sub> as a function of the resonant laser power and read-out time. The solid line is a guide to the eye, and the dashed lines represent projections onto each plane. The top inset shows the measured photon count probability distributions upon probabilistic charge state initialization into NV<sup>-</sup> and NV<sup>0</sup> (bright and dark states, respectively); the extracted read-out fidelity in this case is 98% (Supplementary Section 3). PLE, photoluminescence excitation.

ODMR spectrum under non-resonant red illumination—where both dips are visible (upper trace)—flags NV-selective charge control. Since each ODMR trace involves multiple repeats, these results simultaneously demonstrate our ability to initialize, write and read out the charge state of each NV virtually unlimited times.

While resonant excitation renders NV<sup>-</sup> ionization deterministic (Fig. 1c), the uncertainty associated with each individual charge state read-out is a priori unclear. To address this question, we implemented 'single-shot' charge state detection, and determined the read-out fidelity from the photon count distributions we measured upon NV charge state preparation. The histograms in Fig. 2c show a representative example; probabilistic initialization into NV<sup>-</sup> (~80%) leads to overlap, which, nonetheless, we deconvolve with the aid of post-selection (Methods and Supplementary Section 3). For low laser powers, we attain fidelities reaching up to 98%, limited by spectral diffusion<sup>33</sup>. Increasing the illumination intensity to shorten the read-out also impacts the fidelity, thus leading to a complex interplay. We capture this multi-parameter response through a three-dimensional plot that takes into account the trade-off between laser power and read-out duration. Remarkably, the fidelity remains above 90% even for the shortest read-out times (2 ms), limited by our (non-ideal) photon collection efficiency (Methods).

In Fig. 3, we combine frequency-selective NV imaging and optical spectroscopy to identify a sub-diffraction cluster of four NVs whose optical transitions we map to those expected in the presence of local fields (Fig. 3a–d; also Supplementary Section 4). We demonstrate selective charge control and non-destructive read-out in Fig. 3e. Starting from a state where only  $NV_E$  is neutral (trace ①), we successively bring the red laser frequency on-resonance with the  $NV_D$  and  $NV_C$  transitions to induce selective ionization (respectively traces ② and ③). Unlike in Fig. 2, the process occurs in the absence of green illumination and

hence without resorting to a charge state reset, in the process providing a pathway to discriminating individual NVs in crowded spectra. Additional observations at half-hour intervals confirm the final charge state configuration in the set, though multiple read-outs can lead to unintended ionization (trace ® and Supplementary Section 4); other practical limitations include spectral diffusion and charge initialization (Supplementary Sections 1 and 4).

# Multiplexed storage in NV ensembles

Besides their more complex charge dynamics, denser NV sets lead to congested optical spectra where individually addressing all NVs ultimately becomes impractical. To explore the response of larger NV ensembles, we now turn to crystal B featuring an NV concentration of ~30 parts per 10<sup>9</sup> (ppb), orders of magnitude greater than in crystal A. Given the sub-diffraction average distance between NVs (~60 nm), confocal microscopy cannot discriminate individual contributions, instead yielding featureless images that capture only the mesoscale variations in NV number. Strain and electric fields lead to a broad distribution of optical resonances (~100 GHz; Fig. 4a), though generalizing the experiments of Figs. 2 and 3 to the ensemble is not immediate, as it is not a priori clear that the impact of narrow-band illumination-ionizing the subset of NVs with optical transitions at the laser frequency-can be confined to a spectral range smaller than the full heterogeneous line-width (hence making crosstalk unavoidable). Further, direct examination is needed to assess carrier diffusion and recapture during writing and/or read-out, potentially altering the charge state of previously encoded NVs (Supplementary Section 5).

That these problems can be circumvented is shown in Fig. 4c, where we address groups of NVs with optical transitions centred around optical frequencies spaced every 7 GHz. The result is a collection of 12

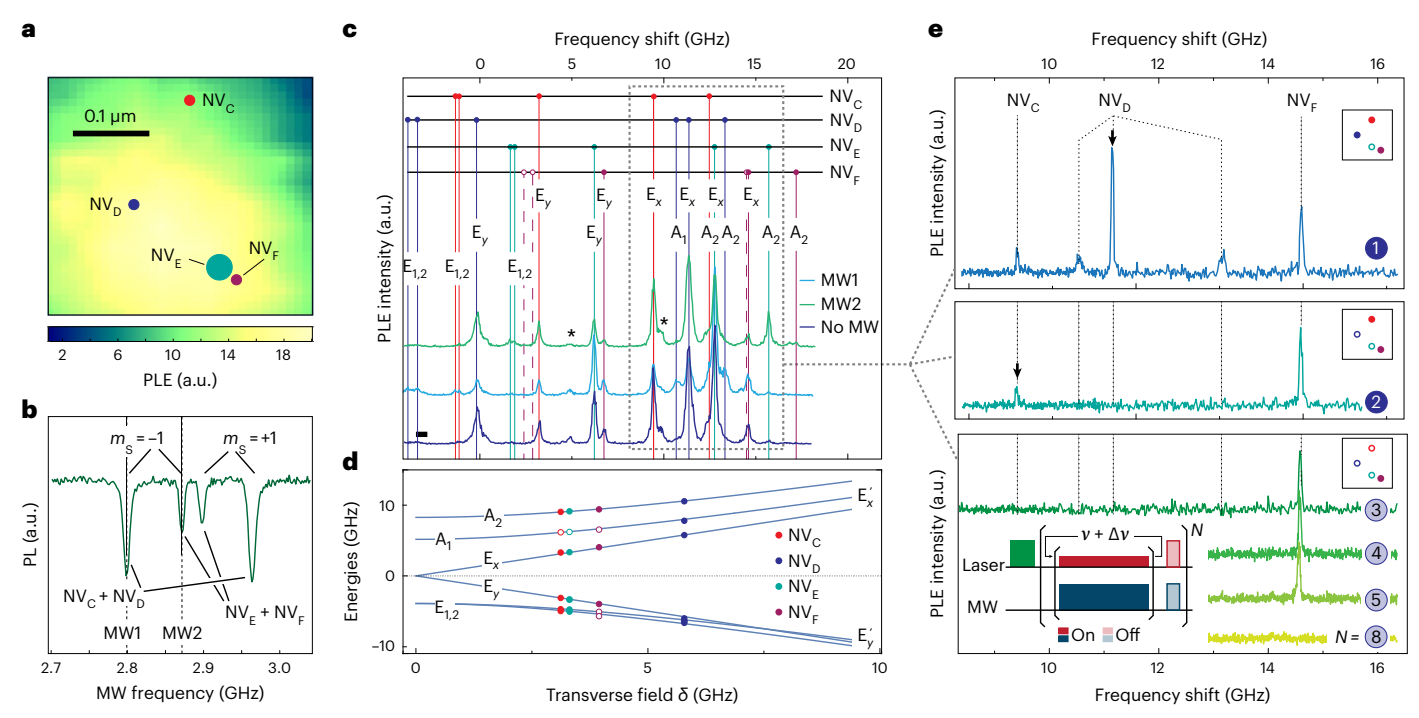


Fig. 3 | Charge manipulation and non-destructive optical spectroscopy of a four-NV sub-diffraction cluster. a, Confocal image of a NV cluster sharing the same diffraction-limited volume. The superimposed circles show the mean positions of each NV as determined from selective excitation; diameters indicate standard deviations (68% confidence intervals). b, c, ODMR and optical spectroscopy of the four-NV cluster using the protocol in Fig. 1b; blue, light blue and green traces illustrate the cluster response in the absence of MW or upon intercalating MW inversion pulses resonant with different ODMR transitions; asterisks mark unassigned PLE peaks, perhaps associated with a fifth NV in the cluster. Empty circles denote weak or unobserved transitions. d, Calculated energies in the NV excited manifold as a function of the transverse electric/strain field  $(\delta)$ . Full circles indicate the measured energies for each NV in the cluster as derived from c. e, Non-destructive optical spectroscopy of the cluster; the

schematic at the lower left shows v denoting laser frequency and  $\Delta v$  as the step during the spectral reconstruction; N is the trace number. In this illustration, green illumination (1  $\mu$ W, 10 s) initializes  $NV_C$ ,  $NV_D$  and  $NV_F$  into the negatively charged state while  $NV_E$  remains neutral and is thus unobservable (trace ①). Traces ② and ③ show the resulting spectra upon ionizing first  $NV_D$  and then  $NV_C$ , respectively, with the laser tuned to the transition indicated by the arrow; full (empty) circles in the upper right insets indicate negative (neutral)  $NV_E$  in the cluster using the colour code in a. Traces ④ and ⑤ are successive non-destructive read-outs of the same charge configuration; trace ⑥ shows the result of unintended ionization of  $NV_F$  during read-out. Throughout these spectra, the red laser power is 5 nW during read-out and 50  $\mu$ W during the 200-ms-long ionization pulses; reconstructing one spectrum typically takes three minutes. In  $\mathbf{c}$  and  $\mathbf{d}$ , the laser frequency shifts are relative to 470.480 THz.

charge-encoded patterns in the same crystal plane with minimal mutual interference. Despite the narrow line-width of an individual optical transition (-100 MHz), unintended crosstalk becomes apparent for narrower frequency steps, hence imposing a practical limit; additional constraints derive from the homogeneity of the NV content and the type and concentration of coexisting charge traps (Supplementary Sections 5–7).

## **Conclusions**

Additional research is needed before these findings can translate into a viable data storage technology, although several features make the present approach of interest. For example, there is arguably no limit on the number of photoactivated charge cycles a NV can undergo; further, since charge control relies on resonant optical excitation, the amount of laser energy required per writing operation is low (-2 nJ for a beam intensity of 0.2 MW cm $^{-2}$ ), especially if compared to STED-based lithography (where the inhibition beam energy is -10 MW cm $^{-2}$  for a writing energy of -1  $\mu$ J at best  $^{21}$ ).

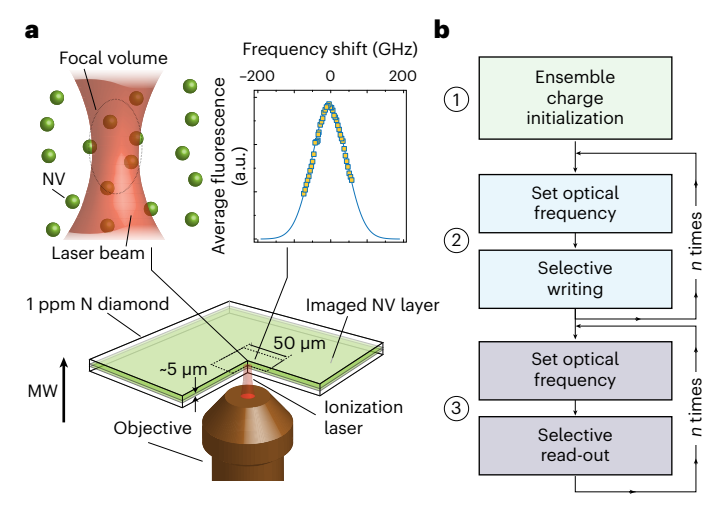
Although rewriting a diffraction-limited volume as presently demonstrated requires reinitialization into  $NV^-$ , selective recombination from a state where all NVs are neutral could potentially be attained via resonant, narrow-band excitation of the strain-induced transitions around 575 nm (ref. 34). Future work may also combine resonant optical excitation with super-resolution methods to better understand the interplay between local electric fields, spatial proximity and selective

optical addressability. Along related lines, material growth techniques could be adapted to produce crystals where the composition and local fields are chosen to optimize NV charge state stability and spectral dispersion<sup>35</sup>. Attaining individual colour centre control throughout these crystals could prove rewarding: for illustration, a NV content of -1 ppb—similar to the local density in Fig. 3—would correspond to a capacity of 2 petabits inch<sup>-3</sup>, which compares favourably with alternative optical storage technologies (Supplementary Section 8).

The present results could find extensions via emitters other than the NV (for example, the SiV centre in diamond) or in other material platforms (such as silicon carbide, hexagonal boron nitride, rare-earth-hosting garnets or silicon). Besides applications to data storage, selectively addressing colour centres separated by sub-diffraction distances could be useful in the investigation of carrier transport between physically distant point defects<sup>36,37</sup> or to study correlated electric noise<sup>38</sup>. Similarly, recent observations in diamond-hosted SiV (ref. 39) and NV (ref. 4) centres suggest the use of resonant near-ionizing excitation to induce bound-exciton Rydberg states; the delocalized, large-radius nature of these orbitals could be exploited as a platform to induce dipole blockading between proximal colour centres, a step towards replicating atomic physics phenomena in the solid state<sup>40</sup>.

#### **Online content**

Any methods, additional references, Nature Portfolio reporting summaries, source data, extended data, supplementary information,



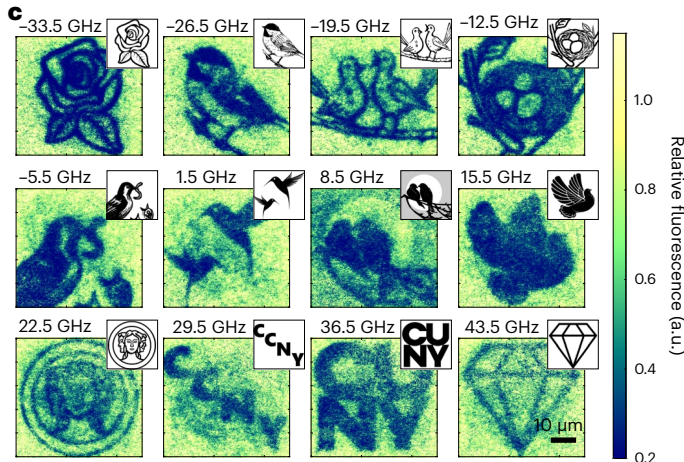


**Fig. 4** | **Multiplexed data storage. a**, We study a [100] type 1b diamond with NV content greater than in crystal A (the top left inset shows a zoomed-in view). Confocal imaging and optical spectroscopy in a section of an inner, 5- $\mu$ m-thick plane reveal an average inter-NV separation below diffraction as well as a broad, strain-induced distribution of optical transitions (top right inset). **b**, Schematics of the data storage protocol. We use a 532 nm scan (61  $\mu$ W) to initialize NVs into the negatively charged state (step ①) followed by band-selective 637 nm illumination (20  $\mu$ W) to write *n* charge-encoded, spatially overlapping patterns (step ②); we implement a similar protocol for data read-out (step ③) except that

we reduce the laser illumination power to 2  $\mu$ W so as to avoid NV ionization. c, Frequency-selective read-out of the in-plane, charge-encoded dataset; the pixel size is  $0.36~\mu\text{m}^2$ , and the read-out time per pixel is 1 ms. The order in the image reconstruction is left to right, top to bottom, hence leading to a gradual loss of contrast (Supplementary Section 5). In a and c, frequency shifts are measured relative to 470.48039 THz; no external magnetic field is present, and MW excitation at the NV zero-field splitting frequency (2.877 GHz) accompanies resonant optical excitation during writing and read-out.

acknowledgements, peer review information; details of author contributions and competing interests; and statements of data and code availability are available at https://doi.org/10.1038/s41565-023-01542-9.

### References

- Degen, C. L., Reinhard, F. & Cappellaro, P. Quantum sensing. Rev. Mod. Phys. 89, 035002 (2017).
- Awschalom, D. D., Hanson, R., Wrachtrup, J. & Zhou, B. B. Quantum technologies with optically interfaced solid-state spins. Nat. Photon. 12, 516–527 (2018).
- Aslam, N., Waldherr, G., Neumann, P., Jelezko, F. & Wrachtrup, J. Photo-induced ionization dynamics of the nitrogen vacancy defect in diamond investigated by single-shot charge state detection. New J. Phys. 15, 013064 (2013).
- Lozovoi, A. et al. Optical activation and detection of charge transport between individual colour centres in diamond. *Nat. Electron.* 4, 717–724 (2021).
- Mizuochi, N. et al. Electrically driven single-photon source at room temperature in diamond. Nat. Photon. 6, 299–303 (2012).
- 6. Lozovoi, A., Vizkelethy, G., Bielejec, E. & Meriles, C. A. Imaging dark charge emitters in diamond via carrier-to-photon conversion. *Sci. Adv.* **8**, eabl9402 (2022).
- Shields, B. J., Unterreithmeier, Q. P., De Leon, N. P., Park, H. & Lukin, M. D. Efficient readout of a single spin state in diamond via spin-to-charge conversion. *Phys. Rev. Lett.* 114, 136402 (2015).
- Hopper, D. A., Lauigan, J. D., Huang, T.-Y. & Bassett, L. C. Real-time charge initialization of diamond nitrogen-vacancy centers for enhanced spin readout. *Phys. Rev. Appl.* 13, 024016 (2020).
- Jayakumar, H., Dhomkar, S., Henshaw, J. & Meriles, C. A. Spin readout via spin-to-charge conversion in bulk diamond nitrogen-vacancy ensembles. Appl. Phys. Lett. 113, 122404 (2018).
- Zhang, Q. et al. High-fidelity single-shot readout of single electron spin in diamond with spin-to-charge conversion. *Nat. Commun.* 12, 1529 (2021).
- Irber, D. M. et al. Robust all-optical single-shot readout of nitrogen-vacancy centers in diamond. Nat. Commun. 12, 532 (2021).

- Dhomkar, S., Henshaw, J., Jayakumar, H. & Meriles, C. A. Long-term data storage in diamond. Sci. Adv. 2, e1600911 (2016).
- Dhomkar, S., Jayakumar, H., Zangara, P. R. & Meriles, C. A. Charge dynamics in near-surface, variable-density ensembles of nitrogen-vacancy centers in diamond. *Nano Lett.* 18, 4046–4052 (2018).
- 14. Wolfowicz, G. et al. Optical charge state control of spin defects in 4H-SiC. *Nat. Commun.* **8**, 1876 (2017).
- Rittweger, E., Han, K. Y., Irvine, S. E., Eggeling, C. & Hell, S. W. STED microscopy reveals crystal colour centres with nanometric resolution. *Nat. Photon.* 3, 144–147 (2009).
- Huang, B., Wang, W., Bates, M. & Zhuang, X. Three-dimensional super-resolution imaging by stochastic optical reconstruction microscopy. Science 319, 810–813 (2008).
- Pfender, M., Aslam, N., Waldherr, G., Neumann, P. & Wrachtrup, J. Single-spin stochastic optical reconstruction microscopy. *Proc. Natl Acad. Sci. USA* 111, 14669–14674 (2014).
- Rittweger, E., Wildanger, D. & Hell, S. W. Far-field fluorescence nanoscopy of diamond color centers by ground state depletion. *Eur. Phys. Lett.* 86, 14001 (2009).
- Han, K. Y., Kim, S. K., Eggeling, C. & Hell, S. W. Metastable dark states enable ground state depletion microscopy of nitrogen vacancy centers in diamond with diffraction-unlimited resolution. Nano Lett. 10, 3199–3203 (2010).
- Chen, X. et al. Subdiffraction optical manipulation of the charge state of nitrogen vacancy center in diamond. *Light. Sci. Appl.* 4, e230 (2015).
- 21. Lamon, S., Wu, Y., Zhang, Q., Liu, X. & Gu, M. Nanoscale optical writing through upconversion resonance energy transfer. *Sci. Adv.* **7**, eabe2209 (2021).
- 22. Harke, B. et al. Polymerization inhibition by triplet state absorption for nanoscale lithography. *Adv. Mater.* **25**, 904–909 (2013).
- Gan, Z., Cao, Y., Evans, R. A. & Gu, M. Three-dimensional deep sub-diffraction optical beam lithography with 9 nm feature size. Nat. Commun. 4, 2061 (2013).

- Li, L., Gattass, R. R., Gershgoren, E., Hwang, H. & Fourkas, J. T. Achieving λ/20 resolution by one-color initiation and deactivation of polymerization. Science 324, 910–913 (2009).
- Wollhofen, R., Katzmann, J., Hrelescu, C., Jacak, J. & Klar, T. A.
  120 nm resolution and 55 nm structure size in STED-lithography.
  Opt. Express 21, 10831–10840 (2013).
- Fischer, J., von Freymann, G. & Wegener, M. The materials challenge in diffraction-unlimited direct-laser-writing optical lithography. Adv. Mater. 22, 3578–3582 (2010).
- Tamarat, P. H. et al. Spin-flip and spin-conserving optical transitions of the nitrogen-vacancy centre in diamond. New J. Phys. 10, 045004 (2008).
- Manson, N. B., Harrison, J. P. & Sellars, M. J. Nitrogen-vacancy center in diamond: model of the electronic structure and associated dynamics. *Phys. Rev. B* 74, 104303 (2006).
- Maze, J. R. et al. Properties of nitrogen-vacancy centers in diamond: the group theoretic approach. New J. Phys. 13, 025025 (2011).
- 30. Doherty, M. W. et al. The nitrogen-vacancy colour centre in diamond. *Phys. Rep.* **528**, 1–45 (2013).
- Sipahigil, A. et al. Indistinguishable photons from separated silicon-vacancy centers in diamond. *Phys. Rev. Lett.* 113, 113602 (2014).
- 32. Bersin, E. et al. Individual control and readout of qubits in a sub-diffraction volume. *npj Quant. Inf.* **5**, 38 (2019).
- 33. Fu, K.-M. C. et al. Observation of the dynamic Jahn-Teller effect in the excited states of nitrogen-vacancy centers in diamond. *Phys. Rev. Lett.* **103**, 256404 (2009).
- Baier, S. et al. Orbital and spin dynamics of single neutrallycharged nitrogen-vacancy centers in diamond. *Phys. Rev. Lett.* 125, 193601 (2020).

- Edmonds, A. M. et al. Characterization of CVD diamond with high concentrations of nitrogen for magnetic-field sensing applications. *Mater. Quant. Technol.* 1, 025001 (2021).
- Oberg, L. M. et al. Spin coherent quantum transport of electrons between defects in diamond. *Nanophotonincs* 8, 1975–1984 (2019).
- 37. Doherty, M. W. et al. Towards a room-temperature spin quantum bus in diamond via optical spin injection, transport and detection. *Phys. Rev. X* **6**, 041035 (2016).
- 38. McCullian, B. A., Cheung, H. F. H., Chen, H. Y. & Fuchs, G. D. Quantifying the spectral diffusion of N-V centers by symmetry. *Phys. Rev. Appl.* **18**, 064011 (2022).
- 39. Zhang, Z.-H. et al. Optically detected magnetic resonance in neutral silicon vacancy centers in diamond via bound exciton states. *Phys. Rev. Lett.* **125**, 237402 (2020).
- Kazimierczuk, T., Fröhlich, D., Scheel, S., Stolz, H. & Bayer, M. Giant Rydberg excitons in the copper oxide Cu<sub>2</sub>O. *Nature* 514, 343–347 (2014).

**Publisher's note** Springer Nature remains neutral with regard to jurisdictional claims in published maps and institutional affiliations.

Springer Nature or its licensor (e.g. a society or other partner) holds exclusive rights to this article under a publishing agreement with the author(s) or other rightsholder(s); author self-archiving of the accepted manuscript version of this article is solely governed by the terms of such publishing agreement and applicable law.

© The Author(s), under exclusive licence to Springer Nature Limited 2023, corrected publication 2024

#### Methods

#### **Experimental set-up**

Throughout our experiments, we use a home-built confocal microscope<sup>41</sup> with excitation in the green (532 nm) and the red (637 nm). We merge the laser beams into a single excitation path with a 605 nm short-pass filter onto a single mode fibre. We produce laser pulses with the aid of acousto-optic modulators with a 10 ns rise time, and detect NV fluorescence via a single-photon avalanche photodetector. Long-pass filters and a 650 nm dichroic mirror allow us to reject laser excitation leaking into the detection path. We use a permanent magnet to create a small magnetic field (4 mT) close to the vacuum chamber, and a cryo-workstation (Montana Instruments) to control the sample temperature down to 5 K. Inside the vacuum chamber sits an air objective (×100 Zeiss Epiplan Neofluar with a numerical aperture of 0.75). We use a tunable laser diode (Toptica DL pro HP 637) for resonant excitation, which we stabilize (±200 MHz absolute accuracy) with a wavemeter (High-Finesse WS/6-200). We control the NV electron's spin via pulsed MW excitation produced by two signal generators (Rhode & Schwarz SMB100A and Stanford Research Systems SG386) and gate either signal via radio frequency switches from Minicircuits; a PulseBlaster transistor-transistor logic (TTL) pulse generator controls the timing of all pulses in our protocols. A 25 µm copper wire overlaid on the sample serves as the MW source in protocols demanding spin manipulation.

#### Sample details

Experiments on single NV centres use a (100), electronic-grade diamond crystal from Element6. Experiments on ensembles, on the other hand, rely on a (100) diamond from DDK with approximately 1 ppm of nitrogen and estimated NV content of 30 ppb. Unlike other similar crystals from the same vendor, this particular crystal shows no traces of SiV centres.

#### Measurement protocols

Individual NV ionization. For NV-selective ionization measurements, we charge-initialize NVs via a 1.6 mW, 1-µs-long laser pulse (532 nm) followed by a 210 µW, 100 µs light pulse (637 nm) for selective ionization. Both NVs exhibit similar Rabi frequencies of 9.09 MHz for the chosen MW field strength at their respective  $|0\rangle\leftrightarrow|1\rangle$  transitions in the ground triplet. To reconstruct the ODMR spectra in Fig. 2b, we monitor the system photoluminescence as we sweep the MW frequency for a variable (but fixed) ionization pulse wavelength. The increase in spin contrast for the non-ionized NV stems from a decrease in fluorescence upon ionization of the other NV. Throughout these experiments, the magnetic field has a magnitude  $B=4.51\pm0.05$  mT; from the observed  $|0\rangle\leftrightarrow|\pm1\rangle$  ODMR resonance dips, we conclude<sup>42</sup> that B forms angles  $\theta_{\text{NV}_1}=28.8\pm1.14$  deg and  $\theta_{\text{NV}_2}=105.9\pm0.19$  deg with respect to NV<sub>1</sub> and NV<sub>2</sub>, respectively.

Charge state read-out fidelity of individual NVs. To characterize the charge state read-out fidelity, we use an initialization read-out sequence comprising a green laser pulse (100 μW for 10-1,000 μs), a short red laser pulse for data post-selection (100-1,000 µs) and a longer red laser pulse for charge read-out. The same sequence is implemented only with the red laser to determine the NV<sup>0</sup> state read-out fidelity. For a given red laser power, we choose the post-selection pulse length such that ionization can be neglected compared to other read-out errors. The post-selection criteria are then chosen to bring the initialization error to the same level, keeping only 8-25% of the cases. Finally, the photon threshold between the bright and dark read-outs is taken such as to simultaneously maximize the fidelity of the bright-state read-out (post-selected data) and dark-state read-out (red-only sequence). For a given red laser power (50–500 nW), we choose the duration of the red laser read-out pulse (20-400 ms) so as to maximize those fidelities, with durations generally close to the defect average ionization time. These parameters are then used on the non-selected data to determine the bright-state initialization fidelity (79% in the single NV case). In order to build enough statistics, sequences are typically repeated 10,000 and 5,000 times for the bright and dark states, respectively.

**NV ensemble imprint.** To initialize the background to a bright NV state, we perform a  $61 \,\mu\text{W}$ ,  $532 \,\text{nm}$  scan with 1 ms dwell time per pixel. Then, we use a 20  $\mu$ W, 637 nm laser to imprint patterns with dwell times varying from 2 ms to 500 ns for greyscale images. For multiplexed imaging, NV<sup>-</sup> bright-state initialization is performed once. Following each imprint, we use the wavemeter to stabilize the laser frequency at the next desired frequency. After imprinting all desired images, we use a weak 2 µW laser for read-out at each chosen frequency. All images contain 300 pixels × 300 pixels in a 50 × 50 µm<sup>2</sup> window. Throughout these experiments, we apply no external magnetic field. To prevent spin depletion, we accompany resonant optical excitation at 637 nm with a strong MW excitation at 2.877 GHz that equilibrates spin populations between all levels in the ground triplet. Continuous MW excitation increases the sample temperature by <1 K. To reconstruct the photoluminescence excitation spectrum in Fig. 4a, we conduct a spatial average over a  $(50 \, \mu m)^2$  area in an inner diamond plane.

# **Data availability**

The data that support the findings of this study are available from the corresponding author upon reasonable request.

#### References

- 41. Monge, R. et al. Spin dynamics of a solid-state qubit in proximity to a superconductor. *Nano Lett.* **23**, 422–428 (2023).
- 42. Balasubramanian, G. et al. Nanoscale imaging magnetometry with diamond spins under ambient conditions. *Nature* **455**, 648–651 (2008).

#### **Acknowledgements**

We acknowledge useful discussions with D. Irber, F. Reinhard and A. Lozovoi. R.M. and C.A.M. acknowledge support from the National Science Foundation through grant NSF-1914945; T.D. and C.A.M. acknowledge support from the National Science Foundation through grant NSF-2216838. R.M. acknowledges support from NSF-2316693. We all acknowledge the access to the facilities and research infrastructure of the National Science Foundation CREST IDEALS, grant NSF-2112550.

#### **Author contributions**

R.M., T.D. and C.A.M. conceived the experiments. R.M. and T.D. conducted the experiments and analysed the data with C.A.M.'s assistance. C.A.M. supervised the project and wrote the manuscript with input from all authors.

#### **Competing interests**

The authors declare no competing interests.

#### **Additional information**

**Supplementary information** The online version contains supplementary material available at https://doi.org/10.1038/s41565-023-01542-9.

**Correspondence and requests for materials** should be addressed to Carlos A. Meriles.

**Peer review information** *Nature Nanotechnology* thanks the anonymous reviewers for their contribution to the peer review of this work.

**Reprints and permissions information** is available at www.nature.com/reprints.